



## Insights into CO<sub>2</sub> Adsorption and Chemical Fixation Properties of Hf-VPI-100 Metal-Organic Frameworks

Journal:	<i>Journal of Materials Chemistry A</i>
Manuscript ID	TA-ART-07-2018-006383.R1
Article Type:	Paper
Date Submitted by the Author:	24-Aug-2018
Complete List of Authors:	Zhu, Jie; Virginia Polytechnic Institute and State University, Chemistry Liu, Jianzhao; Virginia Tech, Chemistry Machain, Yered; Virginia Tech, Chemistry Bonnett, Brittany; Virginia Tech, Chemistry Lin, Shaoyang; Virginia Tech, Chemistry; Virginia Tech, Cai, Meng; Virginia Tech, Chemistry Kessinger, Matthew; Virginia Tech, Chemistry Usov, Pavel; Virginia Tech, Chemistry Xu, Wenqian; Argonne National Laboratory, X-ray Science Division Senanayake, Sanjaya; Brookhaven National Laboratory, Chemistry Troya, Diego; Virginia Tech Esker, Alan; Virginia Tech, Chemistry Department Morris, Amanda; Virginia Tech, Chemistry

## Insights into CO<sub>2</sub> Adsorption and Chemical Fixation Properties of VPI-100 Metal-Organic Frameworks

Received 00th January 20xx,  
Accepted 00th January 20xx

DOI: 10.1039/x0xx00000x

www.rsc.org/

Jie Zhu,<sup>a</sup> Jianzhao Liu,<sup>a</sup> Yered Machain,<sup>a</sup> Brittany Bonnett,<sup>a</sup> Shaoyang Lin,<sup>a</sup> Meng Cai,<sup>a</sup> Matthew C. Kessinger,<sup>a</sup> Pavel M. Usov,<sup>a</sup> Wenqian Xu,<sup>b</sup> Sanjaya D. Senanayake,<sup>c</sup> Diego Troya,<sup>a</sup> Alan R. Esker,<sup>a</sup> Amanda J. Morris<sup>\*a</sup>

Metal-organic frameworks (MOFs) have shown great promise as efficient CO<sub>2</sub> adsorbents, as well as an emerging class of heterogeneous catalysts for conversion of CO<sub>2</sub> to other useful chemicals. In this work, we synthesized and characterized two isostructural hafnium-based MOFs, denoted as Hf-VPI-100 (Cu) and Hf-VPI-100 (Ni). Both frameworks demonstrated high catalytic efficiency for cycloaddition of CO<sub>2</sub> to epoxides under ambient pressure. *In situ* PXRD, QCM and DRIFTS have been used to probe the interaction between the guest molecules (CO<sub>2</sub>/epoxide) and Hf-VPI-100. The crystal structures of these frameworks were preserved during the exposure to CO<sub>2</sub> atmosphere up to 20 bar. The epoxide uptake per unit cell of VPI-100 and diffusion coefficients have been calculated by QCM analysis. Comparison of catalytic efficiency between Hf-VPI-100 and the previously reported Zr-based VPI-100, aided by electronic structure calculations revealed that the open metal centers in the metallocyclam act as the primary Lewis acid sites to facilitate the catalytic conversion of CO<sub>2</sub>.

### 1. Introduction

The rise of anthropogenic CO<sub>2</sub> emissions<sup>1</sup> has triggered a series of environmental problems, including global climate change<sup>2</sup> and ocean acidification.<sup>3</sup> As a result, our ability to manage and mitigate this by-product of industrial civilization will become increasingly important for combating these issues. An attractive option is to utilize CO<sub>2</sub> as a chemical feedstock to produce a variety of important materials and chemical intermediates. While this approach is unlikely to usefully reduce the CO<sub>2</sub> concentration in the atmosphere, it nevertheless targets a vast reservoir of inexpensive, renewable and non-toxic C1 resources.<sup>4-8</sup> One of the most effective examples of CO<sub>2</sub>'s chemical utilization is its cycloaddition reaction with epoxide, a highly atom-economical reaction with minimal by-products. The products of this chemical transformation, cyclic carbonates, find many applications, including polar aprotic solvents, electrolytes for lithium-ion batteries, and valuable intermediates for polycarbonate and polyurethane synthesis.<sup>9-10</sup> Therefore, extensive research has focused on the development of efficient heterogeneous catalysts to promote these transformations.<sup>11-14</sup> In particular, metal-organic frameworks (MOFs) are promising candidates for this application, due to their high internal surface area, chemical and structural tunability, high density of accessible catalytic sites, and high affinity towards CO<sub>2</sub>.<sup>6, 15-18</sup>

The mechanism for the cycloaddition of CO<sub>2</sub> to epoxides

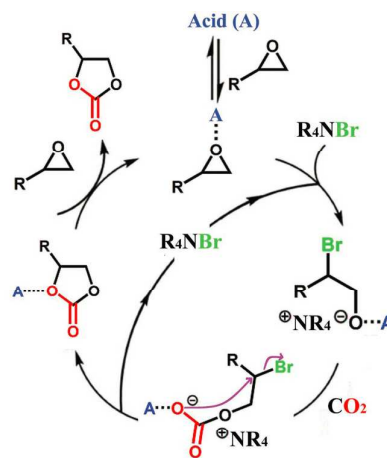


**Fig. 1** Proposed mechanism for the acid-catalysed (A) cyclic carbonate synthesis from epoxides and CO<sub>2</sub> in the presence of a tetraalkylammonium halide (bromide).

typically involves an acid catalyst (such as a metal ion or a proton) that activates epoxide for subsequent nucleophilic attack by the co-catalyst (typically a tetraalkylammonium halide) to form a haloalkoxide. This intermediate further reacts with CO<sub>2</sub> through cycloaddition liberating cyclic carbonate product and regenerating the tetraalkylammonium halide co-catalyst (Figure 1).<sup>15, 19</sup> Therefore, the reported catalytic MOFs usually contain structural defects, -OH hydrogen-bond donors, open metal sites from metal nodes (secondary building unit; SBU), and/or linkers to serve as Lewis acid sites. Although different active sites in MOFs have been proposed based on the mechanism mentioned above, it is generally difficult to precisely identify the location where the catalysis occurs

<sup>a</sup> Department of Chemistry, Virginia Tech, Blacksburg, VA 24061, United States.  
E-mail: [ajmorris@vt.edu](mailto:ajmorris@vt.edu); Tel: +1 540 231 5585

<sup>b</sup> X-ray Science Division, Advanced Photon Source, Argonne National Laboratory, Argonne, Illinois 60439, United States.

<sup>c</sup> Department of Chemistry, Brookhaven National Lab, Upton, NY, United States.  
Electronic Supplementary Information (ESI) available: [details of any supplementary information available should be included here]. See DOI: 10.1039/x0xx00000x

inside the framework, especially when multiple Lewis acid sites are available in the same material.

The ambiguity in determining the dominant reaction centre is readily apparent in zirconium MOFs with metallo-ligands. The nodes, depending on ligand connectivity, can feature both terminal and bridging hydroxides, which can act as Brønsted acid centres and engage cyclic epoxides via hydrogen-bond formation, thereby activating the addition of CO<sub>2</sub>. The hydroxide-mediated mechanistic pathway was investigated in detail by Farha et al. in a comparative study between the Zr and Hf analogues of NU-1000 (Hf-NU-1000).<sup>20</sup> Computational studies predicted that the hydroxyl protons on the Hf analogue were slightly more acidic than those on the Zr analogue, supporting the superior catalytic performance of Hf-NU-1000 at mild conditions compared to that of NU-1000. Zhou et al. reported the catalytic activity of PCN-224 (Co) toward the chemical transformation.<sup>21</sup> PCN-224 (Co) features both hydroxide-terminated nodes and a porphyrin metallo-ligand, both of which could activate epoxides. Control experiments with the non-metallated ligand did not provide clear evidence of the actual active site (node vs. metallo-porphyrin), as the protonated, free-base porphyrin can also engage epoxide in hydrogen bonds, much as the SBU's hydroxide ligands. Interestingly, despite the potential to provide active site determination, the interactions between epoxide/CO<sub>2</sub> and the internal MOF environment has not been explored in detail in previous reports.

We recently reported the synthesis and reactivity of VPI-100 toward the catalytic transformation of epoxides.<sup>22</sup> VPI-100 is characterized by zirconium oxide/hydroxide nodes and metallo-cyclam ligands, representing a dual active site MOF. In this paper, we aim to answer the question as to the identity of the dominant reactive site in the VPI-100 series. To do so, we prepared and characterized hafnium analogues of VPI-100 MOFs (Hf-VPI-100). These structures are composed of Lewis acid containing linkers (metallo-cyclams) and active metal oxide/hydroxide nodes (Hf<sub>6</sub>). The interaction between epoxide/CO<sub>2</sub> and the framework was probed by *in situ* powder X-ray diffraction (PXRD), diffuse reflectance infrared Fourier transform spectroscopy (DRIFTS), quartz crystal microbalance (QCM) studies, and electronic structure calculations. These materials demonstrated high CO<sub>2</sub> uptake under ambient pressure and maintained structural integrity under 20 bar of CO<sub>2</sub>. The irreversible uptake of epoxide by the VPI-100 MOFs has been revealed by QCM, which indicates relatively strong binding between the epoxide and the frameworks. Coupled to the experimental data, the *ab initio* calculations helped identify the metal centres in the cyclam linkers as the dominant active sites for the epoxide activation.

## 2. Results and discussion

### 2.1 Synthesis and characterization

Similar to previously reported VPI-100 MOFs, the Hf-VPI-100 analogues were prepared using two-step modulated synthetic strategy.<sup>23</sup> Formic acid was used as the modulator to pre-form the hafnium oxo-cluster in the first step, followed by the reaction with the metallo-cyclam ligands.<sup>22</sup> Hf-VPI-100 (Cu) and Hf-VPI-100 (Ni) were obtained as violet and light pink crystalline powders, respectively, matching the appearances to the corresponding Zr frameworks. SEM images revealed the morphology of the MOF samples as quasi-spherical particles with diameters of 30-100 nm (Figure S3). Powder X-ray diffraction (PXRD) patterns (Figure 2A)

collected using a synchrotron radiation source at the Argonne National Laboratory Beamline 17-BM showed that Hf-VPI-100 (Cu) and Hf-VPI-100 (Ni) are isostructural. Peak indexing and Rietveld

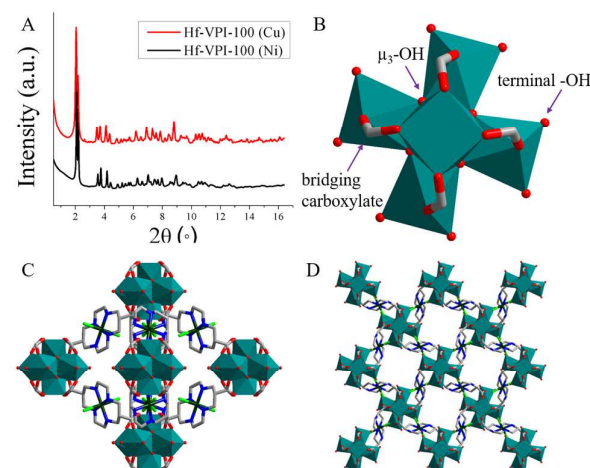


**Fig. 2** (A) PXRD patterns of as-synthesized Hf-VPI-100 MOFs collected at room temperature. (B) The structure of the discrete Hf<sub>6</sub> cluster, as viewed down the c axis. (C) Schematic structure of Hf-VPI-100 (Ni). (D) Packing diagram viewed down the c axis. Colour scheme: Hf, teal; Cu, grey; O, red; N, blue, Ni, dark green; Cl, green.

analysis (Figure S1 and S2) confirmed that these frameworks have the same overall crystal structures (Figure 2), with a slight difference in unit cell parameters. Both MOFs crystallize in the I4/m space group with the same molecular formula, [Hf<sub>6</sub>(μ<sub>3</sub>-OH)<sub>8</sub>(OH)<sub>8</sub>(ML)<sub>4</sub>], where M = Cu<sup>2+</sup>/Ni<sup>2+</sup>, L = 6,13-dicarboxy-1,4,8,11-tetrazacyclotetradecan. Similar to other 8-connected Zr-MOFs, such as PCN-222,<sup>24</sup> each Hf<sub>6</sub> cluster is capped with eight μ<sub>3</sub>-OH ligands. Eight of the twelve octahedral edges are connected to cyclam ligands, while the remaining Hf sites are occupied by eight terminal -OH ligands (Figure 2B). Moreover, comparison of experimental PXRD patterns between Hf-VPI-100 and the parent VPI-100 showed that the Hf and Zr analogues are isostructural (Figure S4).

The XPS spectra revealed the oxidation states of metals inside the Hf-VPI-100 MOFs to be Hf(IV), Ni(II), and Cu(II) (Figures S5 and S6), which is consistent with VPI-100. FT-IR spectra further confirmed the overall structural similarity of the VPI-100 analogues (Figure S7). Compared with metal-cyclam linkers, the carboxylic acid stretches in Hf-VPI-100 MOFs exhibited a redshift (from 1614 to 1585 cm<sup>-1</sup>) due to the chelation of oxygen atoms to Hf<sub>6</sub> clusters, which serve as a primary structural link. Thermogravimetric analysis (TGA) of the activated sample (Figure S8) showed that ligand loss occurred at 270 and 330 °C for Hf-VPI-100 (Cu) and Hf-VPI-100 (Ni), respectively. The Ni framework displayed higher thermal stability than the Cu analogue, which was further confirmed by variable temperature *in situ* PXRD. A similar trend has been also reported in Zr-based VPI-100 MOFs. The porosity of Hf-VPI-100 MOFs was studied by N<sub>2</sub> adsorption-desorption experiments at 77 K with both frameworks exhibiting reversible type II isotherms (Figure S9). Brunauer-Emmett-Teller (BET) surface areas of 396 m<sup>2</sup> g<sup>-1</sup> and 399 m<sup>2</sup> g<sup>-1</sup> were calculated from N<sub>2</sub> isotherms for Hf-VPI-100 (Cu) and Hf-VPI-100 (Ni), respectively. Fourier Transform and Monte Carlo simulations revealed the pore diameters followed the same trend, 7.7 Å and 7.2 Å.

## 2.2 Catalytic studies – Cycloaddition of CO<sub>2</sub> to epoxides

Hf-VPI-100 (Cu) and Hf-VPI-100 (Ni) were investigated as heterogeneous catalysts for cycloaddition of CO<sub>2</sub> to epoxides in the presence of tetrabutylammonium bromide (TBAB) as co-catalyst under relatively low CO<sub>2</sub> pressure (1.5 bar). In a typical catalysis experiment, the Hf-VPI-100 powder (0.008 mmol), co-catalyst TBAB (0.31 mmol), and an epoxide (31.3 mmol) were placed in a 20 mL stainless steel autoclave reactor. The catalytic reaction was carried out at 90 °C and 1.5 bar CO<sub>2</sub> for 6 h, and the resulting mixture was analysed by <sup>1</sup>H NMR to determine the conversion yield and the selectivity of cycloaddition products (Supporting information, Section 3).<sup>25</sup> For epoxide substrates, epichlorohydrin (boiling point = 118 °C) and 1,2-epoxybutane (boiling point = 63 °C) were selected due to their lack of volatility, which precludes the evaporation of unreacted epoxide during the workup procedure and thus, minimized inaccuracy in yield calculations.

**Table 1** Cycloaddition of CO<sub>2</sub> and epichlorohydrin run in the presence of different catalysts<sup>a</sup>

Catalyst	Run	Yield (%) <sup>b</sup>
TBAB	----	16.2
[CuL(CIO <sub>4</sub> ) <sub>2</sub> ] and TBAB	----	90.2
Hf-VPI-100 (Cu) and TBAB	1	97.2
Hf-VPI-100 (Cu) and TBAB	2	95.6
Hf-VPI-100 (Ni) and TBAB	1	89.5
Hf-VPI-100 (Ni) and TBAB	2	86.2

<sup>a</sup> Reaction conditions: 31.3 mmol epoxide, 0.008 mmol Hf-VPI-100 MOF and 0.31 mmol TBAB (1% mol) under 1.5 bar CO<sub>2</sub> and 90 °C for 6 h. <sup>b</sup> Conversion was evaluated from the <sup>1</sup>H NMR spectra by integration of epoxide versus cyclic carbonate peaks. (Figure S9 - 14)

As shown in Table 1, Hf-VPI-100 demonstrated high catalytic activity for cycloaddition of epichlorohydrin and CO<sub>2</sub>. At relatively mild conditions (1.5 bar CO<sub>2</sub>, 90 °C, 6 h) yields were 95(±2)% and 90(±3)% for Cu and Ni analogues, respectively. Control experiments performed without the MOF catalyst and only TBAB present led to a low yield of 16.2%. In the absence of the TBAB co-catalyst, no conversion was detected for the cycloaddition reaction. Moreover, Hf-VPI-100 (Cu) outperformed the Cu(II)-cyclam ligand, which was run as molecular catalyst control and achieved 90% yield for the formation of cyclic carbonate under the same reaction conditions. We reasoned that the catalytic efficiency of molecular catalyst was limited by its low solubility in the epoxide substrates.<sup>22</sup> In contrast, the heterogeneous MOF catalyst contains more accessible active Lewis acid sites inside its structure.

Additionally, the Hf-VPI-100 MOFs demonstrated recyclability. The frameworks were straightforwardly separated from the reaction and reused without substantial loss of catalytic activity, Table 1. The recycled MOF powders retained their crystallinity, as evidenced by the retention of the major diffraction peaks compared with the MOF sample before catalysis (Figure S16). ICP-MS analysis of the reaction mixture filtrate revealed no metal ions leached from the sample during the reaction, indicating the MOF did not dissolve/degrade under the reaction conditions. The ICP results also confirm that the catalytic reaction is heterogeneous in nature.

Given that the yields for epichlorohydrin are close to 100% within the time-frame of the reactivity, we chose to investigate CO<sub>2</sub> chemical fixation with 1,2-epoxybutane under the same conditions (1.5 bar CO<sub>2</sub>, 90 °C, 6 h). For this substrate, Zr-based VPI-100 MOFs exhibited lower catalytic conversions compared to

epichlorohydrin.<sup>22</sup> Therefore, clear trends could be observed between the Hf and Zr VPI-100 analogues, as opposed to concerns that reaction times should be adjusted. A similar decrease in yield compared to those for epichlorohydrin was observed for the Hf-VPI-100 analogues. Both Hf-VPI-100 (Cu) and Hf-VPI-100 (Ni) demonstrated higher catalytic activity than the TBAB control (Figure S21) towards the formation of butylene carbonate with a yield of 43.8% and 39.4%, respectively (Figures S17 and 18). Interestingly, similar conversion yields were obtained using Zr-VPI-100 using the same reaction conditions (Figure S19 and 20), despite the Hf node being more oxophilic than the Zr node. This observation suggests that activation of epoxides proceeds through coordination to the open metal centres on the cyclam ligand, as opposed to the node. To probe such a hypothesis, the interactions of CO<sub>2</sub>/epoxide were investigated with *in situ* powder X-ray diffraction (PXRD), diffuse reflectance infrared Fourier transform spectroscopy (DRIFTS), quartz crystal microbalance (QCM) studies, and electronic structure calculations.

## 2.3 Carbon Dioxide – MOF Interaction

The CO<sub>2</sub> capture properties of the Hf-VPI-100 MOFs were investigated at 273 K and 296 K under ambient pressure (Figure 3). Both MOFs exhibited characteristic type I isotherms indicative of microporous materials. The Hf-based materials reached a CO<sub>2</sub> uptake capacity of 42 cm<sup>3</sup> g<sup>-1</sup> (8.3 wt%) and 46 cm<sup>3</sup> g<sup>-1</sup> (9.1 wt%) at 273 K for Hf-VPI-100 (Cu) and Hf-VPI-100 (Ni), respectively. Compared with VPI-100 under the same activation and measurement conditions, the hafnium analogues exhibited significant increase in CO<sub>2</sub> uptake capability (Table S2). This

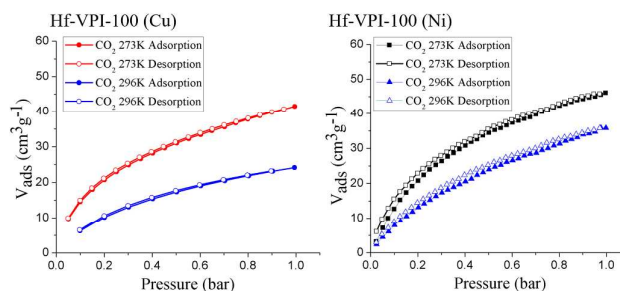


**Fig. 3** CO<sub>2</sub> adsorption isotherms of Hf-VPI-100 MOFs at 273 K and 296 K.

behaviour is attributed to the more polarized nature of  $\mu_3$ -OH groups around Hf<sub>6</sub> clusters, which strengthens the interactions between CO<sub>2</sub> and MOFs.<sup>26</sup>

To probe the specific interaction between CO<sub>2</sub> and Hf-VPI-100 MOFs, *in situ* PXRD experiments were performed under CO<sub>2</sub> atmosphere. Powder patterns of Hf-VPI-100 under helium and CO<sub>2</sub> from 1 to 20 bar were collected at 298 K. As shown in Figure 4, no significant phase change has been observed, as evident from the high degree of similarity between diffraction patterns of both frameworks under He and 20 bar of CO<sub>2</sub>. For Hf-VPI-100 (Cu), two small peaks ( $2\theta = 2.8$  and  $3.1^\circ$ ) emerged in the presence of CO<sub>2</sub> in the low angle region. The peak intensity gradually increased with the increase of CO<sub>2</sub> pressure. A similar change was also observed in the PXRD data of Hf-VPI-100 (Ni), as shown in the inset of Figure 4. The two emerging peaks are attributed to the electronic density change after CO<sub>2</sub> diffused into the pore of Hf-VPI-100. However, the

weak nature of this band precluded further analysis to determine the specific binding sites between CO<sub>2</sub> and the framework. DRIFTS experiments were also conducted. No signal change was observed except for the appearance of vibrational peaks due to gaseous CO<sub>2</sub>. Therefore, no specific chemical binding sites for CO<sub>2</sub> inside Hf-VPI-100 could be conclusively identified from these measurements. Notwithstanding, the *in situ* PXRD and DRIFTS measurements confirmed that the Hf-VPI-100 MOFs maintained their crystal structure under a CO<sub>2</sub> atmosphere up to 20 bar.

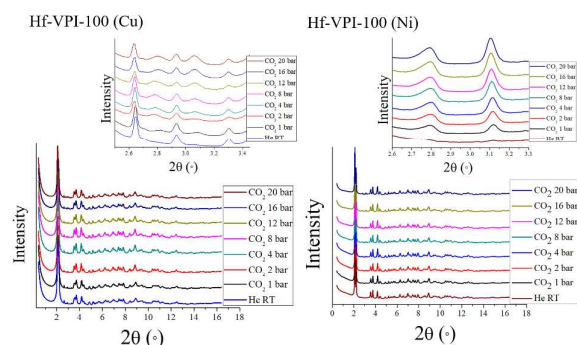


Fig. 4 *In situ* PXRD patterns of Hf-VPI-100 under He and CO<sub>2</sub> from 1 bar to 20 bar.

#### 2.4 Epoxide – MOF Interaction

The sorption kinetics of 1,2-epoxybutane onto and into MOF systems were studied through QCM experiments. Figure 5 contains representative data for the interaction of 1,2-epoxybutane with two suspension-cast films of Hf-VPI-100 (Cu) at 21 °C. In Figure 5, the resonant frequency ( $\Delta f$ ) divided by the overtone number ( $n$ ) and change in dissipation ( $\Delta D$ ) are plotted for the fifth overtone ( $n = 5$ ) as a function of time. The initial flat region of the plot from a time of zero to approximately 15 min represented a flow of nitrogen gas over the MOF-coated sensor. At approximately 15 min, the flow of nitrogen was diverted through a saturator cell containing 1,2-epoxybutane at a temperature of 18 °C for a relative humidity of ~87% 1,2-epoxybutane. During this step,  $\Delta f/n$  decreased. According to the Sauerbrey equation,<sup>27</sup> a decrease in frequency is proportional to an increase in surface concentration ( $\Gamma$ ) for uniform films with small  $\Delta D$ :

$$\Gamma = -C \left( \frac{\Delta f}{n} \right) \quad (1)$$

where  $C$  is a constant ( $0.177 \text{ mg}\cdot\text{m}^{-2}\cdot\text{Hz}^{-1}$ ) for the 5 MHz crystals used in this study. Thus, exposure of the film to 1,2-epoxybutane caused an uptake of the substrate by the MOF. The flow of 1,2-epoxybutane was continued until  $\Delta f/n$  decreased no further. At approximately 140 min, nitrogen flow through the saturator cell was terminated and only nitrogen flowed over the film. While  $\Delta f/n$  increased rapidly, an indication of desorption of reversibly adsorbed 1,2-epoxybutane,  $\Delta f/n$  did not return to zero. Thus, some of the 1,2-epoxybutane remained irreversibly adsorbed in the film. Enhanced dissipation observed during and after 1,2-epoxybutane uptake (Figure 5B) was interpreted as a softening of the film and a more viscoelastic layer. During the terminal desorption stage, the films hardened as 1,2-epoxybutane left the system but were still softer than the as prepared MOF films due to irreversible uptake of 1,2-epoxybutane.

Experiments like those depicted in Figure 5 were performed for three other MOF based systems: Hf-VPI-100 (Ni), Zr-VPI-100 (Ni), and Zr-VPI-100 (Cu). These systems also demonstrated irreversible adsorption. Values of  $\Delta f/n$  obtained from the end of the experiment and Eq. 1 yielded an estimate of surface concentration for the 1,2-epoxybutane irreversibly adsorbed within the film, ( $\Gamma_{\text{epoxide}}$ ). Using the frequencies of the crystals prior to and after suspension casting, it was also possible to use Eq. 1 to estimate the surface concentration for the MOF film ( $\Gamma_{\text{MOF}}$ ). Combining  $\Gamma_{\text{epoxide}}$  and  $\Gamma_{\text{MOF}}$  along with their respective molar masses,  $M_{\text{epoxide}}$  and  $M_{\text{MOF}}$ , yielded a ratio of epoxide molecules per MOF unit cell:

$$\theta = \frac{\Gamma_{\text{epoxide}}/M_{\text{epoxide}}}{\Gamma_{\text{MOF}}/M_{\text{MOF}}} \quad (2)$$

Values of  $\theta$  are summarized in Table 2. The data exhibited an interesting trend: Zr-VPI-100 (Ni)  $\approx$  Hf-VPI-100 (Ni) > Zr-VPI-100 (Cu) > Hf-VPI-100 (Cu). The MOF films containing Ni had a much stronger affinity for 1,2-epoxybutane and exhibited significantly greater irreversible uptake.

As seen in Figure 5 for the time between 15 and 140 min, rapid and slower uptake processes were clearly present. Assuming Fickian diffusion, sorption into a thin film can yield diffusion coefficients. Fick's second law may be integrated under a thin film condition, i.e. a thin sheet geometry of

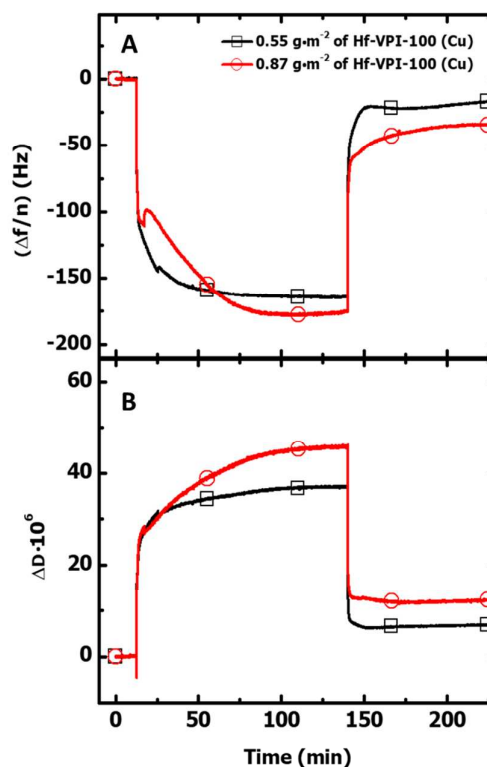


Fig. 5 Representative sorption/desorption curves for 1,2-epoxybutane interacting with Hf-VPI-100 (Cu) thin films. (A)  $\Delta f/n$  vs. time and (B)  $\Delta D$  vs. time. Curves correspond to the fifth overtone.

thickness  $L$ , neglecting diffusion through the edges to yield,<sup>28-29</sup>

$$\frac{\Gamma(t)}{\Gamma_{\infty}} = 1 - \frac{8}{\pi^2} \sum_{m=0}^{\infty} \frac{1}{(2m+1)^2} \exp\left(-\frac{D(2m+1)^2\pi^2 t}{L^2}\right) \quad (3)$$

where  $\Gamma_{\infty}$  represents the maximum surface concentration before the final purge of nitrogen gas and  $\Gamma(t)$  is the surface concentration at a given time  $t$ . The thickness of thin film,  $L$ , is calculated by the surface concentration ( $\Gamma_{\text{MOF}}$ ) and the density ( $\rho_{\text{MOF}}$ ) for the MOF film

**Table 2** QCM results for  $\theta$ ,  $D_1$  and  $D_2$  for VPI-100-MOFs<sup>a</sup>

	Hf-VPI-100 (Cu)	Hf-VPI-100 (Ni)	Zr-VPI-100 (Cu)	Zr-VPI-100 (Ni)
$\theta_{\text{epoxide/MOF}}$	0.23±0.06	0.68±0.04	0.47±0.05	0.71±0.08
$D_1 \cdot 10^{10} \text{ (cm}^2\text{s}^{-1}\text{)}$	5.2±2.5	7.4±1.6	0.47±0.09	6.5±3.5
$D_2 \cdot 10^{12} \text{ (cm}^2\text{s}^{-1}\text{)}$	1.1±0.5	1.8±0.5	0.49±0.14	1.9±0.7

<sup>a</sup> Average of two films ± one standard deviation

$$L = \frac{\Gamma_{\text{MOF}}}{\rho_{\text{MOF}}} \quad (4)$$

In the early adsorption stages, for constant  $D$  and  $L$ , Eq. 3 can be simplified as<sup>29</sup>

$$\frac{\Gamma(t)}{\Gamma_{\infty}} \approx \frac{4}{\sqrt{\pi}} \sqrt{\frac{Dt}{L^2}} \quad (5)$$

Following the approach of others working with MOF or polymer systems,<sup>28, 30-31</sup> Eq. 1 was assumed, and the experimental data were converted to  $\Gamma$  values. According to Eq. 5,  $D$  values can be estimated from plots of  $\Gamma$  as a function of the square root of  $t$ . A representative plot of  $\Gamma$  vs.  $t^{1/2}$  is provided as Figure 6 to highlight the two different diffusion regimes. As seen in Figure 6, the faster sorption mode characterized by the diffusion coefficient  $D_1$  accounted for nearly 2/3 of the total uptake in just 1.5 min, whereas the slower sorption mode characterized by the diffusion coefficient  $D_2$  covered most of the remaining uptake over the period of approximately an hour. Application of Eq. 5 to the two different sorption regimes in Figure 6 for all the films studied yielded the average diffusion coefficients summarized in Table 2. Diffusion coefficients in the faster sorption regime ( $D_1$ ) were at least 100 times greater than in the slower sorption regime ( $D_2$ ) for all systems. The Zr-VPI-100 (Cu) system exhibited significantly slower diffusion than the other systems in both sorption regimes. Experimental diffusion coefficients for other MOFs have been reported, and range from  $6 \times 10^{-15} \text{ cm}^2\text{s}^{-1}$  (cyclohexane sorption into HKUST-1) to  $6 \times 10^{-9} \text{ cm}^2\text{s}^{-1}$  (ferrocene diffusion into  $\text{Cu}_2(\text{ndc})_2(\text{dabco})$ ).<sup>30-34</sup> For the fast sorption regime,  $D_1 \sim 10^{-10} \text{ cm}^2\text{s}^{-1}$  are consistent with the diffusion of xylene into UiO-66.<sup>32</sup> For the slow sorption regime,  $D_2 \sim 10^{-12} \text{ cm}^2\text{s}^{-1}$  are in accordance with the diffusion of ferrocene vapor into HKUST-1.<sup>33</sup>

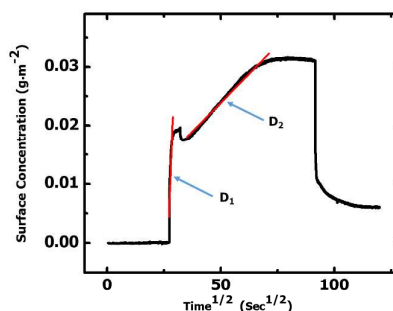


**Fig. 6** Representative data of surface concentration vs. square root of time for the adsorption of 1,2-epoxybutane onto a Hf-VPI-100 (Cu) thin film ( $\Gamma_{\text{MOF}} \sim 0.87 \text{ g}\cdot\text{m}^{-2}$ ).

As seen from Table 2, VPI-100 MOF thin films with Ni cyclams have higher 1,2-epoxybutane to MOF unit cell ratios. This trend is consistent with DFT calculations (M06-2X/def2TZVP) of epoxide binding to Ni(II) and Cu(II) cyclams, which indicate binding to Ni(II) is 11 kJ/mol more exothermic than on Cu(II). Based upon Table 2, the mobility within VPI-100 MOF thin film and 1,2-epoxybutane is Hf-VPI-100 (Ni)  $\approx$  Zr-VPI-100 (Ni)  $\approx$  Hf-VPI-100 (Cu)  $>$  Zr-VPI-100 (Cu).

Taken together, the  $\theta$  and diffusion data indicate that there is a specific interaction between the MOF and the epoxide. Both the metal-cyclam identity dependence and similar values for  $\theta$  between the Hf and Zr analogues support that the epoxide binds to the metal cyclam under the experimental conditions. Interestingly, Zr/Hf-VPI-100 (Cu) displayed a lower  $\theta$  compared to Zr/Hf-VPI-100 (Ni). Additionally, the diffusion coefficients for both the fast and slow diffusion processes also follow this trend, faster diffusion through Zr/Hf-VPI-100 (Ni). We attribute both the higher  $\theta$  and faster diffusion through the Ni analogue compared to Cu to the presence of bound counter-balancing ions on the metallo-cyclam core. Refinement of the crystal structures indicates metal to chloride ratios of 2:1.64 for Ni:Cl and 2:2.68 for Cu:Cl (Table S1). The remaining Cl required for charge balance is un-bound and located within the MOF pore environment. For full occupancy of the axial sites, the ratios should be 2:4. Averaged over the MOF structure each nickel is occupied by 0.81 Cl and the Cu by 1.34. In terms of  $\theta$ , Zr/Hf-VPI-100 (Ni) simply has

## ARTICLE

Journal Name

more open sites to bind epoxide. For the trend in diffusion, it is proposed that the bound Cl would occlude the pores thus negatively impacting diffusion.

### 2.5 Computational Insight

To obtain fundamental atomistic insight into the cycloaddition reaction, we enlisted electronic structure calculations. The calculations focused on the key ring-opening step of the activated epoxide, which in this work is elicited by bromide. The essential question we aimed to answer is whether there is a significant difference between epoxide activation by the metal centre in the cyclam linkers and by the Hf-OH moiety in the SBU. Epoxide activation at the linkers involves direct coordination of the epoxide to the Lewis-acid metal centre, while, as described in prior work with Hf-NU-1000, activation by Hf-OH at the SBU is via hydrogen-bond formation with the epoxide. This fundamental difference in substrate coordination in fact served as a central motivation in the design of VPI-100, as introduction of metal cyclam linkers affords the potential for rich substrate-metal chemistry nor readily available at the SBU or with other non-metal linkers.

The calculations indeed reveal significant differences in the epoxide ring-opening barriers by bromide following activation at the cyclam metal centres or at the SBU. This is shown in Figure 7, where the barriers are segregated according to activation mode (coordinate-covalent binding at the cyclam or hydrogen bond). For hydrogen-bond activation, we have considered an SBU Hf-OH moiety as a donor, as well as the NH group of a Ni-cyclam linker with two Cl counterions. Irrespective of the choice of hydrogen-bond donor, we find that binding of the epoxide to coordinatively unsaturated Ni(II) or Cu(II) sites in the cyclam linker dramatically lowers bromide's nucleophilic addition barrier, by more than 75 kJ/mol. Interestingly, the lower barrier demands of cyclam epoxide activation can be roughly followed by the length of the forming bond at the transition state, which signals a preference toward earlier transition states compared to hydrogen bond activation.

The vastly lower barriers for epoxide ring opening via activation at the cyclam rather than at the SBU provide atomistic understanding for the insensitivity of the CO<sub>2</sub> experimental conversion yield from Zr-VPI-100 to Hf-VPI-100. Since low-barrier reaction localizes at the cyclams, changes to the SBU metal should play a minor role. These computational results also nicely substantiate the rationale for metal incorporation into the VPI-100 linkers, which diverts reactivity from the nodes to the more strongly Lewis-acidic linker sites and opens the possibility of more diverse chemistry within the MOF.

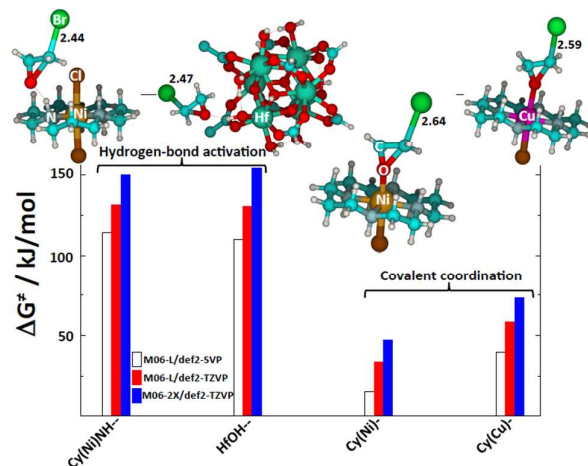


Fig. 7 Calculated epoxide ring-opening barriers by bromide (298 K) for various activation modes. Numbers represent distances of the forming bond at the transition state in angstrom.

### 3. Conclusions

In summary, the mechanism of the addition of CO<sub>2</sub> to epoxides by VPI-100 was probed and support for activation of the epoxide by the metal cyclam was provided. Hf-VPI-100 analogues were prepared via modulated synthesis and the reactivity of the Zr-VPI-100 and Hf-VPI-100 MOFs compared. The frameworks exhibited comparable reaction yields for cyclams of the same identity, i.e. Hf/Zr-VPI-100 (Cu) yields were 43.8% and 55.3%; Hf/Zr-VPI-100 (Ni) yields were 39.4% and 40.3%, respectively. Thus, it was postulated that the activation of epoxides occurs via a metal-cyclam mediated process, as opposed to a node-mediated process.

To provide further insight, the interactions between the MOFs and the reaction components – epoxide and CO<sub>2</sub> – were investigated. *In situ* PXRD, revealed no specific binding site between CO<sub>2</sub> and Hf-VPI-100, despite the emergence of peaks due to electron density attributed to CO<sub>2</sub> sorption. However, the differences in gas uptake (Zr-VPI-100 (Cu/Ni) – 6.65 and 5.52 wt% vs. Hf-VPI-100 (Cu/Ni) – 8.25 and 9.13 wt%) between the Hf-VPI-100 and Zr-VPI-100 analogues indicated that the nodes dominate the CO<sub>2</sub> sorption behavior. QCM was used to probe the interaction between 1,2-epoxybutane and the frameworks. The uptake of 1,2-epoxybutane and the diffusion coefficients for two adsorption processes have been obtained from quantitative analysis in QCM. The results indicate a strong binding interaction between the MOF and the epoxide. More importantly, the results support that the MOF-epoxide interaction occurs at the metal cyclam. DFT calculations revealed that the open metal sites in the metallo-cyclam are more potent Lewis-acid sites for epoxide activation than the Brønsted acid hydroxyl sites on the metal-oxide nodes. Thus, the presented work provided critical mechanistic insight that will enable the development of efficient MOF catalysts for the chemical fixation of CO<sub>2</sub>. Interestingly, the results indicate that the CO<sub>2</sub> sorption and epoxide activation parameters can be tuned independently to maximize catalytic efficiency, a strategy that is the focus of future study.

## 4. Experimental

### 4.1 Materials

All chemicals were purchased from commercial sources and used without further purification unless otherwise mentioned.

**Caution!** The perchlorate salts described are potentially explosive and should be handled with care and prepared in small quantities.

### 4.2 Synthesis

**Synthesis of 6,13-dicarboxy-1,4,8,11-tetrazacyclotetradecan-copper (II) perchlorate [CuL(ClO<sub>4</sub>)<sub>2</sub>] (1).** Based on our reported procedure,<sup>22</sup> the tetracarboxylate precursor [Cu(tetach<sub>4</sub>)](ClO<sub>4</sub>)<sub>2</sub> (0.63 g, 0.99 mmol) was added to 10 mL of 0.1 M HClO<sub>4</sub> solution and heated at reflux for 1 h. After the reaction mixture cooled down to room temperature (R.T.), 3 mL of 60% HClO<sub>4</sub> was added and the solution refrigerated overnight. The product was filtered off as red crystalline solid (0.38 g, 46% yield). The structure of [CuL(ClO<sub>4</sub>)<sub>2</sub>] was shown in Figure S22.

**Synthesis of 6,13-dicarboxy-1,4,8,11-tetrazacyclotetradecan (L) (2).** Based on our reported procedure,<sup>22</sup> the free-base ligand (2) was prepared by the demetallation of (1). The [CuL(ClO<sub>4</sub>)<sub>2</sub>] (0.32 g, 0.58 mmol) was added to 20 mL of 37% HCl and heated to reflux for 1 h. The resultant white solid was filtered and washed with ethanol. After drying under vacuum, white powder (0.16 g, 95% yield) was obtained. (ESI-MS: [M-H]<sup>+</sup> m/z = 289.19)

**Synthesis of Hf-VPI-100 (Cu).** The Hf-VPI-100 (Cu) was prepared using a similar approach as reported for VPI-100 MOFs.<sup>22</sup> In an 8 mL vial, HfCl<sub>4</sub> (19 mg, 0.06 mmol) was added in 4 mL of dry DMF with 0.44 mL (200 eq.) of formic acid. The vial was heated at 80 °C in an oven for 1 h. After cooling to R.T., [CuL(ClO<sub>4</sub>)<sub>2</sub>] (33 mg, 0.06 mmol) was added and the solution was sonicated for 10 min. Then, the mixture was heated in a 120 °C oven for 24 h. After cooling to R.T., the crystalline solid was isolated by centrifugation, rinsed with fresh DMF and acetone. The powder was dried under vacuum at 60 °C. Violet crystalline powder was obtained (30 mg, 76% yield). The phase purity of Hf-VPI-100 (Cu) was verified by PXRD.

**Synthesis of Hf-VPI-100 (Ni).** The Hf-VPI-100 (Ni) was prepared using a similar approach as reported for VPI-100 MOFs.<sup>22</sup> In an 8 mL vial, HfCl<sub>4</sub> (19 mg, 0.06 mmol) was dissolved in 2 mL of dry DMF with 0.44 mL (200 eq.) of formic acid. In a separate vial, NiCl<sub>2</sub>·6H<sub>2</sub>O (14 mg, 0.06 mmol) and free-base ligand (2) (17.3 mg, 0.06 mmol) were added to 2 mL of dry DMF and sonicated for 10 mins. Then, both vials were heated in an 80 °C oven for 1 h. The solutions were combined into one vial and heated in a 120 °C oven for 24 h. After cooling to R.T., the resultant solid was isolated by centrifugation, washed with fresh DMF and acetone. The product was dried under vacuum at 60 °C. Light pink crystalline powders were obtained (20 mg, 51% yield). The phase purity of Hf-VPI-100 (Ni) was confirmed by PXRD.

### 4.3 Characterization and analysis

**Structure determination and refinement.** The structures of Hf-VPI-100 were determined by PXRD using synchrotron radiation at the Beamline 17-BM at Advanced Photon Source at Argonne National Laboratory. Samples were loaded in a capillary flow cell device and 2D diffraction data were taken in transmission geometry

by a PerkinElmer flat panel area detector.<sup>35</sup> 2D data calibration and integration was performed with software GSAS-II.<sup>36</sup> Structural refinement was carried out with TOPAS v5.

**Powder X-ray Diffraction (PXRD).** The phase purity of the synthesized MOF samples was analyzed on a Rigaku Miniflex diffractometer with a Cu(Kα) radiation (λ = 1.5418 Å) over a 2θ range of 3–50° in continuous scanning mode (1.0°/min) and a resolution of 0.05°. The powder samples were loaded onto a zero-background Si (510) disk.

**Attenuated Total Reflectance Fourier-Transform Infrared Spectroscopy (ATR-FTIR).** ATR-FTIR spectra were obtained using a Varian 670 FT-IR Spectrometer. All spectra were an average of 64 scans for powdered samples and were recorded from 4000 to 500 cm<sup>-1</sup> with 4 cm<sup>-1</sup> resolutions.

**Thermogravimetric Analysis (TGA).** The MOF samples (~5 mg) were placed on a Pt pan and heated at a rate of 10 °C/min under nitrogen atmosphere over the temperature range of 25–600 °C by using a Q500 thermogravimetric analyzer from TA Instruments.

**Scanning electron microscopy imaging (SEM).** Images were collected by using a Leo/Zeiss 1550 Schottky field-emission scanning electron microscope.

**X-ray Photoelectron Spectroscopy (XPS).** The XPS spectra were collected on a PHI 5000 Vera Probe III spectrometer using an aluminium anode X-ray source (photon energy of 1486.6 eV). The pass energy for each scan was set to 69 eV, with a step size of 0.125 eV/step, with signals being averaged over 50 scans for each spectrum.

**N<sub>2</sub>/CO<sub>2</sub> adsorption measurements.** Before a gas sorption experiment, as-synthesized MOF samples (~50 mg) were washed with DMF three times and acetone three times, followed by soaking in acetone for 3 days to allow solvent exchange. The resulting exchanged frameworks were activated under vacuum for 12 h, and then degassed under vacuum for 12 h at 100 °C prior to gas adsorption/desorption measurements. The sorption isotherm data were collected with a Quantachrome Autosorb-1. The surface areas of the samples were determined by fitting the N<sub>2</sub> adsorption data at 77 K within a relative pressure (P/P<sub>0</sub>) range of 0.05 to 0.25 to the BET equation.

**Cycloaddition of CO<sub>2</sub> to epoxides.** Hf-VPI-100 MOF samples (0.008 mmol), tetrabutylammonium bromide (99 mg, 0.31 mmol), and epoxide (31.1 mmol) were added to a 20 mL stainless steel Parr reactor. The sealed vessel was charged with CO<sub>2</sub> (1.5 bar) and heated to 90 °C in an oil bath. After 6 h, the reactor was cooled to R.T. and the unreacted CO<sub>2</sub> was slowly released. A small aliquot was dissolved in CDCl<sub>3</sub> for <sup>1</sup>H NMR analysis to determine the conversion. The reaction solution was centrifuged to recover the catalyst. The recovered MOF powder was washed with CHCl<sub>3</sub> (3 × 1 mL) and dried under vacuum. The sample was reused twice in the catalysis experiment for each substrate. The structural stability of the framework was confirmed by PXRD.

**Quartz Crystal Microbalance (QCM) Experiments.** An E4 quartz crystal microbalance (Q-Sense AB) was used for all QCM experiments. Gold coated QCM sensors with a fundamental frequency of 5 MHz were cleaned by exposure to UV/ozone for 20

min, immersion in a 1:1:5 v/v/v solution of ammonium hydroxide: hydrogen peroxide: water at 80 °C for 1 h, rinsing with ultrapure water and drying with nitrogen. The cleaned sensors were immersed into 3 mM 16-mercaptohexadecanoic acid in ethanol solution for 24 hours to form self-assembled monolayers with terminal carboxylate groups (SAM-COOH). Measurements of the fundamental and overtone frequencies of the SAM-COOH surfaces were taken prior to MOF deposition for subsequent calculation of the total amount of MOF deposited on the crystals. A suspension of MOF particles (0.02~0.07 mg) in ethanol were suspension-cast onto SAM-COOH surfaces. The fundamental frequency and overtones were again measured and the surface concentration of MOF per unit area deposited onto the crystal was calculated from Eq. 1. This method produced a roughly 10% error in  $\theta$  for the MOF.

For gas sorption, experiments followed the work of Grissom et al.<sup>37</sup> The MOF films were held at 21 °C in the QCM cells and purged with nitrogen gas at a constant flow pressure of 4 PSIG relative to the ambient pressure until a stable baseline was obtained. Nitrogen gas was then diverted into a gas saturator cell containing 1,2-epoxybutane held at 18 °C by a water bath that subsequently entered the QCM flow cell. The constant flow of 1,2-epoxybutane vapor continued until the change of frequency reached a stable minimum, which represented the maximum equilibrium uptake. The flow was then switched to pure nitrogen gas, whereby reversibly adsorbed gas could desorb. The process continued until a flat frequency line was observed.

#### 4.4 Computational Studies

Electronic structure calculations were carried out using Gaussian09.<sup>38</sup> Default geometric and electronic convergence criteria were adopted throughout. Geometry optimizations and harmonic frequency analysis were conducted with the M06-L functional,<sup>39</sup> and the def2-SVP basis set.<sup>40</sup> The electronic energy was further refined via single-point calculations at the M06-L/def2-TZVP and M06-2X/def2-TZVP levels. All calculations considered a superfine integration grid and implicit PCM solvation (tetrahydrofuran). To analyse reaction at the cyclam ligands, isolated Cu(II) and Ni(II) 1,4,8,11-tetrazacyclotetradecan species were used in which the metal centres exhibit one chloride counterion and an open site for epoxide coordination. These molecular analogues possess +1 charge and were treated as triplets (Ni) or doublets (Cu). Reaction in which epoxide hydrogen bonds to a Hf-OH moiety in the SBU considered the NU-1000 core with two benzoate linkers directly interacting with epoxide and six formate linkers capping the SBU region removed from the substrate. Xyz coordinates of all optimized structures are provided in the supporting information.

#### 5. Conflicts of interest

There are no conflicts to declare.

#### 6. Acknowledgements

This material is based upon work supported by the U.S. department of Energy, Office of Basic Energy Sciences under Award Number DE-SC0012445. The XPS data was collected on an instrument funded by the National Science Foundation

under award number 1531834. Use of the Advanced Photon Source, an Office of Science User Facility operated for the U.S. Department of Energy (DOE) Office of Science by Argonne National Laboratory, was supported by the U.S. DOE under Contract No. DE-AC02-06CH11357. SDS was supported by the U.S. Department of Energy, Office of Science, Office of Basic Energy Sciences, and Catalysis Science Program under contract No. DE-SC0012704. The authors acknowledge Advanced Research Computing at Virginia Tech for providing computational resources and technical support that have contributed to the results reported within this paper.

#### 7. Notes and references

1. Allen, M. R.; Frame, D. J.; Huntingford, C.; Jones, C. D.; Lowe, J. A.; Meinshausen, M.; Meinshausen, N., *Nature* **2009**, *458*, 1163.
2. Stocker, T., *The Physical Science Basis, Working Group 1*.
3. Orr, J. C.; Fabry, V. J.; Aumont, O.; Bopp, L.; Doney, S. C.; Feely, R. A.; Gnanadesikan, A.; Gruber, N.; Ishida, A.; Joos, F., *Nature* **2005**, *437* (7059), 681.
4. Finn, C.; Schnittger, S.; Yellowlees, L. J.; Love, J. B., *Chem. Commun.* **2012**, *48* (10), 1392-1399.
5. Morris, A. J.; Meyer, G. J.; Fujita, E., *Acc. Chem. Res.* **2009**, *42* (12), 1983-1994.
6. Trickett, C. A.; Helal, A.; Al-Maythalony, B. A.; Yamani, Z. H.; Cordova, K. E.; Yaghi, O. M., *Nat Rev Mater.* **2017**, *2*, 17045.
7. Diercks, C. S.; Liu, Y.; Cordova, K. E.; Yaghi, O. M., *Nat. Mater.* **2018**, *17* (4), 301-307.
8. Yang, H.; Zhang, X.; Zhang, G.; Fei, H., *Chem. Commun.* **2018**, *54* (35), 4469-4472.
9. Cokoja, M.; Bruckmeier, C.; Rieger, B.; Herrmann, W. A.; Kühn, F. E., *Angew. Chem. Int. Ed.* **2011**, *50* (37), 8510-8537.
10. Chen, A.; Zhang, Y.; Chen, J.; Chen, L.; Yu, Y., *J. Mater. Chem. A* **2015**, *3* (18), 9807-9816.
11. James, B. R.; Boissonault, J. A.; Wong-Foy, A. G.; Matzger, A. J.; Sanford, M. S., *RSC Advances* **2018**, *8* (4), 2132-2137.
12. Tharun, J.; Bhin, K.-M.; Roshan, R.; Kim, D. W.; Kathalikkattil, A. C.; Babu, R.; Ahn, H. Y.; Won, Y. S.; Park, D.-W., *Green Chem.* **2016**, *18* (8), 2479-2487.
13. Gao, W.-Y.; Tsai, C.-Y.; Wojtas, L.; Thiounn, T.; Lin, C.-C.; Ma, S., *Inorg. Chem.* **2016**, *55* (15), 7291-7294.
14. Li, X.-Y.; Ma, L.-N.; Liu, Y.; Hou, L.; Wang, Y.-Y.; Zhu, Z., *ACS Appl. Mater. Interfaces* **2018**, *10* (13), 10965-10973.
15. Beyzavi, M. H.; Stephenson, C. J.; Liu, Y.; Karagiari, O.; Hupp, J. T.; Farha, O. K., *Front. Energy* **2015**, *2* (63).
16. He, H.; Perman, J. A.; Zhu, G.; Ma, S., *Small* **2016**, *12* (46), 6309-6324.
17. Maina, J. W.; Pozo-Gonzalo, C.; Kong, L.; Schutz, J.; Hill, M.; Dumeé, L. F., *Mater. Horizons* **2017**, *4* (3), 345-361.
18. Kitagawa, S., *Chem. Soc. Rev.* **2014**, *43* (16), 5415-5418.
19. North, M.; Pasquale, R.; Young, C., *Green Chem.* **2010**, *12* (9), 1514-1539.
20. Beyzavi, M. H.; Klet, R. C.; Tussupbayev, S.; Borycz, J.; Vermeulen, N. A.; Cramer, C. J.; Stoddart, J. F.; Hupp, J. T.; Farha, O. K., *J. Am. Chem. Soc.* **2014**, *136* (45), 15861-15864.
21. Feng, D.; Chung, W.-C.; Wei, Z.; Gu, Z.-Y.; Jiang, H.-L.; Chen, Y.-P.; Darensbourg, D. J.; Zhou, H.-C., *J. Am. Chem. Soc.* **2013**, *135* (45), 17105-17110.
22. Zhu, J.; Usov, P. M.; Xu, W.; Celis-Salazar, P. J.; Lin, S.; Kessinger, M. C.; Landaverde-Alvarado, C.; Cai, M.; May, A. M.; Slebodnick, C.; Zhu, D.; Senanayake, S. D.; Morris, A. J., *J. Am. Chem. Soc.* **2018**, *140* (3), 993-1003.

23. Schaate, A.; Roy, P.; Godt, A.; Lippke, J.; Waltz, F.; Wiebcke, M.; Behrens, P., *Chem. Eur. J.* **2011**, *17* (24), 6643-6651.
24. Feng, D.; Gu, Z. Y.; Li, J. R.; Jiang, H. L.; Wei, Z.; Zhou, H. C., *Angew. Chem.* **2012**, *124* (41), 10453-10456.
25. Guillerm, V.; WeselińskiŁukasz, J.; Belmabkhout, Y.; Cairns, A. J.; D'Elia, V.; WojtasŁukasz; Adil, K.; Eddaoudi, M., *Nat Chem* **2014**, *6* (8), 673-680.
26. Hu, Z.; Peng, Y.; Gao, Y.; Qian, Y.; Ying, S.; Yuan, D.; Horike, S.; Ogiwara, N.; Babarao, R.; Wang, Y.; Yan, N.; Zhao, D., *Chem. Mater.* **2016**, *28* (8), 2659-2667.
27. Sauerbrey, G., *Zeitschrift für Physik* **1959**, *155* (2), 206-222.
28. Aminabhavi, T. M.; Munnolli, R. S., *Polym. Int.* **1994**, *34* (1), 59-72.
29. Crank, J., *The mathematics of diffusion*. Oxford university press: 1975.
30. Zybalyo, O.; Shekhah, O.; Wang, H.; Tafipolsky, M.; Schmid, R.; Johannsmann, D.; Wöll, C., *PCCP* **2010**, *12* (28), 8093-8098.
31. Heinke, L.; Wöll, C., *PCCP* **2013**, *15* (23), 9295-9299.
32. Grissom, T. G.; Sharp, C. H.; Usov, P. M.; Troya, D.; Morris, A. J.; Morris, J. R., *J. Phys. Chem. C* **2018**.
33. Zhou, W.; Wöll, C.; Heinke, L., *Materials* **2015**, *8* (6), 3767-3775.
34. Heinke, L.; Gu, Z. G.; Woll, C., *Nat Commun.* **2014**, *5*, 4562.
35. Chupas, P. J.; Chapman, K. W.; Kurtz, C.; Hanson, J. C.; Lee, P. L.; Grey, C. P., *J. Appl. Crystallogr.* **2008**, *41* (4), 822-824.
36. Toby, B. H.; Von Dreele, R. B., *J. Appl. Crystallogr.* **2013**, *46* (2), 544-549.
37. Grissom, T. G.; Sirrine, J. M.; Long, T. E.; Esker, A. R.; Morris, J. R., *Prog. Org. Coat.* **2017**, *107*, 14-17.
38. Gaussian 09, Revision D.01, M. J. Frisch, G. W. Trucks, H. B. Schlegel, G. E. Scuseria, M. A. Robb, J. R. Cheeseman, G. Scalmani, V. Barone, G. A. Petersson, H. Nakatsuji, X. Li, M. Caricato, A. Marenich, J. Bloino, B. G. Janesko, R. Gomperts, B. Mennucci, H. P. Hratchian, J. V. Ortiz, A. F. Izmaylov, J. L. Sonnenberg, D. Williams-Young, F. Ding, F. Lipparini, F. Egidi, J. Goings, B. Peng, A. Petrone, T. Henderson, D. Ranasinghe, V. G. Zakrzewski, J. Gao, N. Rega, G. Zheng, W. Liang, M. Hada, M. Ehara, K. Toyota, R. Fukuda, J. Hasegawa, M. Ishida, T. Nakajima, Y. Honda, O. Kitao, H. Nakai, T. Vreven, K. Throssell, J. A. Montgomery, Jr., J. E. Peralta, F. Ogliaro, M. Bearpark, J. J. Heyd, E. Brothers, K. N. Kudin, V. N. Staroverov, T. Keith, R. Kobayashi, J. Normand, K. Raghavachari, A. Rendell, J. C. Burant, S. S. Iyengar, J. Tomasi, M. Cossi, J. M. Millam, M. Klene, C. Adamo, R. Cammi, J. W. Ochterski, R. L. Martin, K. Morokuma, O. Farkas, J. B. Foresman, and D. J. Fox, Gaussian, Inc., Wallingford CT, 2016..
39. Zhao, Y.; Truhlar, D. G., *J. Chem. Phys.* **2006**, *125* (19), 194101.
40. Weigend, F.; Ahlrichs, R., *PCCP* **2005**, *7* (18), 3297-3305.